

Check for updates

Dual-Surface Reaction Enabled Organic-Inorganic Hybrid Photodiodes for Faint Light Detection and Imaging

Yibo Zhang, * Gloria Vytas, Haozhe Wang, Dehui Zhang, Jiabao Shen, Chengliang Mao, Rajiv Prinja, Ali Javey, Zheng-Hong Lu,* and Nazir P. Kherani*

Organic-inorganic heterojunction photodetectors are garnering significant research interest. The surface-sensitive nature of nanometer-thin single-crystalline semiconductors vis-à-vis device performance provides an ideal platform for studying organic contacts. Herein, organic-Si nanomembrane (SiNM) hybrid photodetectors are demonstrated for probing faint light and self-powered imaging. Universal approaches to controlling dual-surface reactions are proposed to achieve high-performance devices. A 1,4,5,8,9,11-hexaazatriphenylene hexacarbonitrile (HAT-CN) organic layer effectively blocks electron injection current by reacting to unpin the SiNM surface Fermi level. A low work-function ytterbium oxide (YbO_y) (≈2.9 eV) buffer reduces the hole injection. A facile surface reaction process is systematically optimized for HAT-CN and ytterbium with SiNM to selectively consolidate and deoxidize the natively grown silicon oxide (SiO,), respectively, thereby minimizing noise. Contact interfaces between various dielectrics are investigated for maximizing device performance. The devices achieve competitive performance among state-of-the-art organic-inorganic photodetectors, notably the low noise (sub-pA/µm), ultra-fast microsecond response speed and a high rectification of 3×10^7 . Further, an imaging sensor is demonstrated to operate in self-powered mode. These results provide key insights into interfaces, devices, and system-level applications in organic-inorganic heterogeneous optoelectronics.

1. Introduction

Advancements in semiconductor-oninsulator technology have stimulated the development of nanomembrane optoelectronic devices. These devices benefit from their stable chemical and physical properties, high-quality single-crystalline lattice and excellent compatibility with traditional complementary metal-oxidesemiconductor processes. [1-6] The large surface area associated with a semiconductor nanomembrane and concomitant reduction in photocarrier generation volume result in low photocarrier transition times, facilitating photodetectors with high sensitivity and rapid response speeds.[7-14] These photodetectors have been integrated into both rigid and soft substrates for multiple applications such as health monitoring,[15,16] optical waveguides and lasers, [17,18] bio-sensing, [19,20] digital eyes and imaging,[21,22] and environmental monitoring.[7] Concurrently, over and above traditional homojunctions formed via the diffusion of dopants at high temperatures, [13] numerous materials

Y. Zhang, G. Vytas, H. Wang, J. Shen, R. Prinja, N. P. Kherani The Edward S. Rogers Sr. Department of Electrical and Computer Engineering

University of Toronto

10 King's College Road, Toronto, Ontario M5S 3G4, Canada E-mail: yibojhhk.zhang@mail.utoronto.ca; nazir.kherani@utoronto.ca

Y. Zhang, D. Zhang, A. Javey

Department of Electrical Engineering and Computer Sciences University of California

Berkeley, California 94720, USA

The ORCID identification number(s) for the author(s) of this article can be found under https://doi.org/10.1002/adfm.202516835

© 2025 The Author(s). Advanced Functional Materials published by Wiley-VCH GmbH. This is an open access article under the terms of the Creative Commons Attribution License, which permits use, distribution and reproduction in any medium, provided the original work is properly

DOI: 10.1002/adfm.202516835

Y. Zhang, D. Zhang, A. Javey Materials Sciences Division Lawrence Berkeley National Laboratory Berkeley, California 94720, USA

Materials Chemistry and Nanochemistry Research Group Solar Fuels Cluster Department of Chemistry University of Toronto Toronto, Ontario M5S 3H6, Canada

Z.-H. Lu, N. P. Kherani Department of Materials Science and Engineering University of Toronto

184 College Street, Toronto, Ontario M5S 3E4, Canada

E-mail: zhenghong.lu@utoronto.ca



www.afm-journal.de

have been studied for the development of semiconductor nanomembrane based heterojunction photodetectors. These materials include metals.[14] metal oxides.[23] low-dimensional materials, [24,25] quantum dots, [26] and perovskites. [27] The noise level and the lowest sensed signal are essential parameters for a photodetector. Fittingly, extensive efforts are being made to enhance the photon sensitivity of these heterojunction diodes. One approach integrates light-trapping structures to enhance optical absorption, thereby increasing photo-to-electron conversion.[10,28,29] Another key strategy is reducing the reverse dark current to lower the detection noise and consequently minimize the lowest signal the device can detect with a reasonable signal-to-noise ratio.[30] This noise level is closely related to the surface barrier of the non-injection contact, which is primarily governed by the energy level alignment between the two heterogeneous materials and the interfacial defect states.[31-33]

Organics have been widely employed in commercial applications, impacting vast aspects of modern daily life and the future of optoelectronic technology, ranging from organic lightemission diodes (OLEDs),^[34] organic photodetectors,^[35] organic solar cells,^[36] organic thin-film transistors and organic circuits^[37] to large-area systematic integrations such as artificial skins.^[38] Compared to inorganic materials, these organics offer advantageous properties, including facile and diverse processing routines and a wide range of tunable material properties, such as optical, mechanical, and electrical characteristics.^[39] Specifically, the large span of the material's work function/energy band levels has inspired focused investigations into organic-inorganic heterojunction optoelectronics, such as photodetectors and solar cells based on both bulk and low-dimensional materials.^[39–47]

Organic–Inorganic photodetectors for weak-light detection are emerging research topics based on diverse systems. For example, ultra-fast speed and high detectivity have been achieved in 2D organic–inorganic systems. [47] Meanwhile, scalability and stability remain universal issues limiting their large-area applications. Bulk organic–inorganic heterostructures relying on vertical junctions are easily fabricated for large-scale integration. [39] Their response speed is, however, limited by the low carrier mobility and long transition time for photocarriers generated within the bulk semiconductor layer (following Beer–Lambert's law). Moreover, the full potential of these organic–inorganic heterojunctions has not been unlocked due to the unoptimized contact properties and the resulting ineffective charge carrier injection capability through the contacts.

The highly surface-sensitive nature of single-crystalline semiconductor nanomembranes provides a promising, albeit minimally explored, venue for studying the contact and interface properties of these organics within the framework of organicinorganic hybrid heterojunctions. Meanwhile, efforts to identify suitable contact materials between organics and inorganic nanomembranes, as well as to better understand their interfacial properties, have not yet been thoroughly explored. This is crucial for achieving high detection performance, particularly in sensing faint light with a reasonable response speed, which would benefit a multitude of applications. For a broad range of bulk-thin 2terminal semiconductor devices, dual carrier-transport interfaces dominate the optoelectronic properties. Consequently, optimizing the dual contacts through surface reaction offers a promising strategy to realize giant-performance organic—inorganic heterojunctions, thereby advancing their systematic applications. Here, we simultaneously resolve the challenges above by integrating organics with Si nanomembrane (SiNM) for large-area. scalable and stable organic-inorganic faint-light photodetectors. A commonly explored hole injection layer in OLEDs, 1,4,5,8,9,11hexaazatriphenylene hexacarbonitrile (HAT-CN), with a high work-function and nanometer-thin thickness, is explored as a promising interfacial layer between metal and SiNM that provides strong surface energy band bending in relation to the offset in energy levels. An emerging inorganic material for the electron injection layer, ytterbium oxide (YbO_x), is explored to achieve high-performance Ohmic contact.[48] The condensed photocarrier generation volume for nanometer-thin Si reduces the transition time, thereby enabling a microsecond-fast response speed. Furthermore, the optimized contact at dual-surfaces achieves both mitigated charge injection under reverse bias and high majority carrier injection under forward bias, demonstrating subpA/µm level noise current and a high electrical rectification ratio of up to 3×10^7 . The device can sense pW light with a reasonable signal-to-noise ratio and exhibits over 105 photo-to-dark current ratios under large optical injection. An imager is demonstrated with self-powered operation, indicating promising applications of the surface-reacted organic-inorganic photodiodes. The proposed surface reaction strategies to optimize contacts are expected to be applied to a wide range of emerging materials, including 2D semiconductors, perovskites, and nanomaterials with varying surface conditions and energy bandgaps. Specifically, the observed phenomena related to charge injection and the ensuing discussion are expected to provide general guidance on device optimization for diverse materials and interfaces. The results and insights of this work will inspire and contribute to the development of superior organic-inorganic heterojunctions, enabling innovative optoelectronic devices and applications thereof.

2. Results and Discussion

2.1. Device Structures and Characterization

The device structures and thin-film characterizations are illustrated in Figure 1. The optimized device structure is given in Figure 1a. Deep work-function of HAT-CN organic, together with ≈2 nm silicon oxide (SiO_v), forms a high Schottky barrier with n-SiNM. The ultra-low work-function of YbO_x forms a highperformance Ohmic contact, concurrently blocking hole injection current noise under reverse bias and allowing for giant electron injection under forward bias. The energy band diagram is illustrated in Figure 1b. For the pre-contact diagram, a constant vacuum energy level is indicated to highlight the material energy band offsets. After contact, the induced Si band bending is depicted in Figure 1b. The deep LUMO (lowest unoccupied molecular orbital) level of HAT-CN, along with its high work function, promotes significant upward energy band bending at the Si interface. This effectively blocks electron injection under reverse bias while facilitating the collection of photogenerated holes in the self-powered mode. Additionally, a SiO_x interfacial layer unpins the surface Fermi level, ensuring that the Schottky barrier height is dictated by the energy level alignment between the contact materials (work-function alignment) rather than by high surface state densities.

doi/10.1002/adfm.202516835 by Univ of California

awrence Berkeley National Lab, Wiley Online Library on [16/10/2025]. See the Terms

on Wiley Online Library for rules of use; OA articles are governed by the applicable Creative Commons License

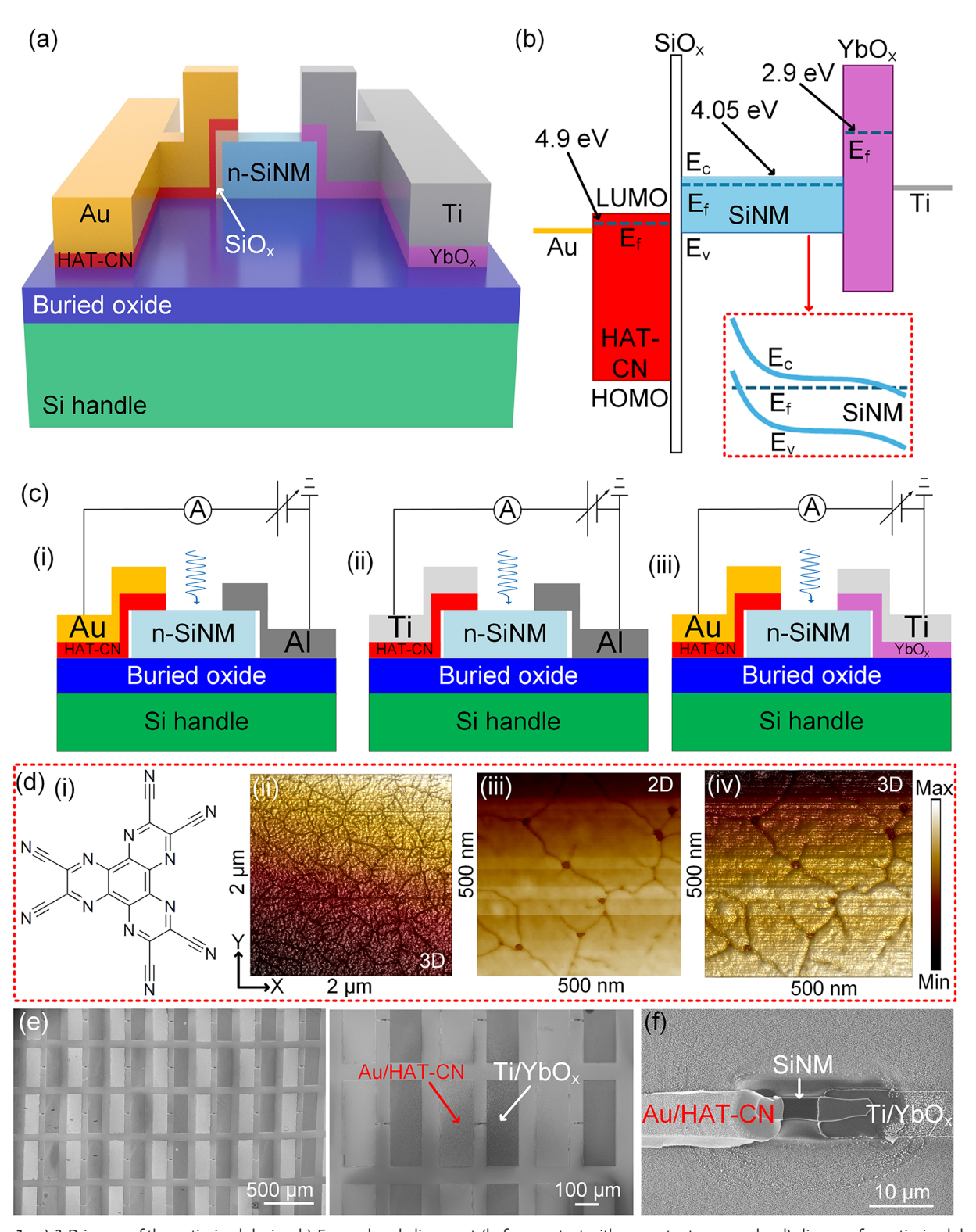


Figure 1. a) 3-D image of the optimized device. b) Energy band alignment (before contact with a constant vacuum level) diagram for optimized device, with an inset showing SiNM surface energy band bending after contact. HOMO: highest occupied molecular orbital. c) Investigated device structures for device optimization. i) HAT-CN/SiNM heterojunction with high work-function Au plate on HAT-CN and Al high-resistance Ohmic contact. ii) HAT-CN/SiNM heterojunction with low work-function Ti plate and Al high-resistance Ohmic contact. iii) HAT-CN/SiNM heterojunction with high work-function Au plate and optimized Ti/YbO_x low-resistance Ohmic contact. d) Surface morphology characterization of HAT-CN. i) HAT-CN molecular structure. ii) Large area ($2 \mu m \times 2 \mu m$) 3-D AFM image for HAT-CN thin film on an SOI substrate. iii) Small area ($500 nm \times 500 nm$) 2-D AFM image. iv) Small area ($500 nm \times 500 nm$) 3-D AFM image. e) SEM image for an array of organic-inorganic heterojunction photodiodes with Au/HAT-CN and Ti/YbO_x contacts. f) SEM image for the device channel region.



www.afm-journal.de

Figure 1c explores various combinations of contact materials for device design. This work proposes and validates three types of heterojunction devices to show the performance optimization process. We begin with an unoptimized n-SiNM device featuring an aluminum (Al) Ohmic contact, as shown in Figure 1c-i. It is suggested that Al forms a slight Schottky barrier with n-SiNM, leading to an upward surface energy band bending. This, in turn, increases contact resistance and affects electron injection under forward bias. For the other contact, a high work-function Au plate is used in conjunction with an HAT-CN buffer layer. The HAT-CN layer forms a strong Schottky barrier with n-SiNM, effectively blocking electron injection under reverse bias. Additionally, a ≈2 nm SiO_x layer is maintained at the organic-inorganic interface to chemically passivate the n-SiNM surface, thereby reducing the photocarrier recombination rate and mitigating reversebias noise. To further investigate the impact of encapsulating metal selection on the carrier injection effect, a low work-function Ti plate is deposited on top of the HAT-CN layer, as shown in Figure 1c-ii. This set of devices demonstrates that surface energy band bending is primarily governed by the HAT-CN buffer layer, with minimal influence from the encapsulating metal. Modifying the interface with nanometer-thin organic layers presents a viable approach to tuning current injection at the contact. By varying the thickness of the HAT-CN layer, a transition between Schottky and Ohmic contact is observed, offering a promising method for adjusting the rectification properties of a contact system. To further optimize the Ohmic contact, Ti/YbO, is used to replace Al as shown in Figure 1c-iii. Upon contact with n-SiNM, the low workfunction YbO_x layer facilitates electron transfer into the n-SiNM surface, inducing downward band bending and forming a lowresistance Ohmic contact. This low contact resistance enables a significant majority carrier injection under forward bias, simultaneously suppressing hole injection current (from the Ohmic contact Fermi level to the n-SiNM valence band) under reverse bias and thereby reducing device noise.

Atomic force microscopy (AFM) is utilized to characterize the surface morphology of HAT-CN thin films in Figure 1d. The molecular structure of HAT-CN is illustrated in Figure 1d-i. A large-area 3D AFM scan (2 $\mu m \times 2 \mu m$) in Figure 1d-ii reveals that the thin HAT-CN film forms separate islands with distinct boundaries. To further examine the surface characteristics, a smaller scanned area (500 nm × 500 nm) is provided in Figure 1d-iii. (2D image) and Figure 1d-iv (3D image), demonstrating a low surface roughness of ≈1.2 nm within a typical island region. A 2D AFM image of a larger thin-film area is given in Figure S1 (Supporting Information). Scanning electron microscopy (SEM) images are presented in Figure 1e,f, illustrating the device structure. A low-magnification SEM image in Figure 1e takes a large-area view of the devices, highlighting the excellent uniformity achieved through the developed physical vapor deposition process for organic films. The fabricated devices feature asymmetrical contacts, with an effective SiNM channel length of less than 10 µm, facilitating rapid separation and collection of photocarriers, as shown in the zoomed-in SEM image in Figure 1f. One challenge encountered during fabrication was the poor adhesion of the organic thin film to the SiO₂ (buried oxide) layer. To address this, slight over-etching of the buried oxide layer was applied during the reactive ion etching (RIE) process, creating nanostructures in the SiO₂ region to improve adhesion.

The SEM image of an individual device is provided in Figure S2 (Supporting Information).

2.2. Device Interface and Material Characterization

The device interface and material properties are analyzed in Figure 2. High-resolution transmission electron microscopy (HRTEM) images depict the Au/HAT-CN/SiO_v/SiNM interface in Figure 2a,b. The focused ion beam process for HRTEM sample preparation is given in Figure S3 (Supporting Information), which also reveals the rough SiO₂ surface. Figure 2a examines the low-magnification cross sectional image of the organic-SiNM junction. The contact material conformally attaches to the SiNM surface. The interface is further revealed by a high-magnification image as shown in Figure 2b. There is no clear boundary between the HAT-CN and SiO_x layers due to a similar Z-contrast between these two dielectrics, and no clear lattice fringes can be observed for the entire \approx 6 nm-thick HAT-CN/SiO $_{\rm x}$ layer. The lattice diffraction pattern of the entire structure is displayed as an inset in Figure 2b. The dominant dot array corresponds to the single crystalline Si lattice, while no lattice dots are witnessed for HAT-CN or SiO_v. This indicates that the HAT-CN/SiO_v layer is amorphous, which agrees with the X-ray diffraction (XRD) results in Figure S4 (Supporting Information). For HAT-CN thin films deposited on a Si-on-insulator (SOI) substrate, only Si peaks are observed from its XRD patterns, confirming the amorphous crystalline nature of HAT-CN. Note that the strong Si peaks may overlap with the HAT-CN signals from XRD measurements, causing suspicions about determining the HAT-CN crystallinity. The HRTEM image primarily confirms the amorphous nature of HAT-CN in Figure 2b and that in Figure S5 (Supporting Information) - no clear HAT-CN lattice is evident. The Ohmic contact is optimized by altering the surface with an ultra-low workfunction YbO, layer, permitting an enormous injection of majority electrons. The HRTEM image for the Ti/YbO_x/SiNM interface is shown in Figure 2c. No clear SiO, is detected underneath the YbO_x layer, advising that the oxygen in the existing SiO_x was replaced by highly reactive Yb, forming YbO_x and Si. This surface reaction reduces the device series resistance by eliminating the high-resistive SiO_v layer and generating a downward surface energy band bend for an electron accumulation layer, as illustrated in Figure 1b. Yb reacting with SiO_x is further investigated by examining the SiNM surfaces with/without YbOx in Figure S6 (Supporting Information). Around 2 nm amorphous layer displaying white color contrast is obtained from the non-YbO, region, demonstrating the presence of SiO, when there is no YbO_x deposited on top. This reaction is energetically favorable due to the high Gibbs free energy of Yb, since it is more likely to react with oxygen to form oxides than Si. The elemental interdiffusion and the reaction at the Au/HAT-CN/SiO_v/SiNM interface are confirmed by electron energy loss spectroscopy (EELS) mapping results in Figure 2d. A line boundary is displayed for the Au mapping result, signifying that Au diffuses into HAT-CN. The oxygen and Si distribution results validate the existence of SiO, with a thickness of ≈ 2 nm. The SiO, layer chemically passivates the SiNM surface, reducing leakage current and enhancing photocarrier collection rates by suppressing recombination. The overall composite image also confirms that Au diffuses into

16163028, 0, Downloaded from https://advanced.onlinelibrary.wiley.com/doi/10.1002/adfm.202516835 by Univ of California

awrence Berkeley National Lab, Wiley Online Library on [16/10/2025]. See the Terms and Conditions (https://onlinelibrary.wiley_

on Wiley Online Library for rules of use; OA articles are governed by the applicable Creative Commons License

www.afm-journal.de

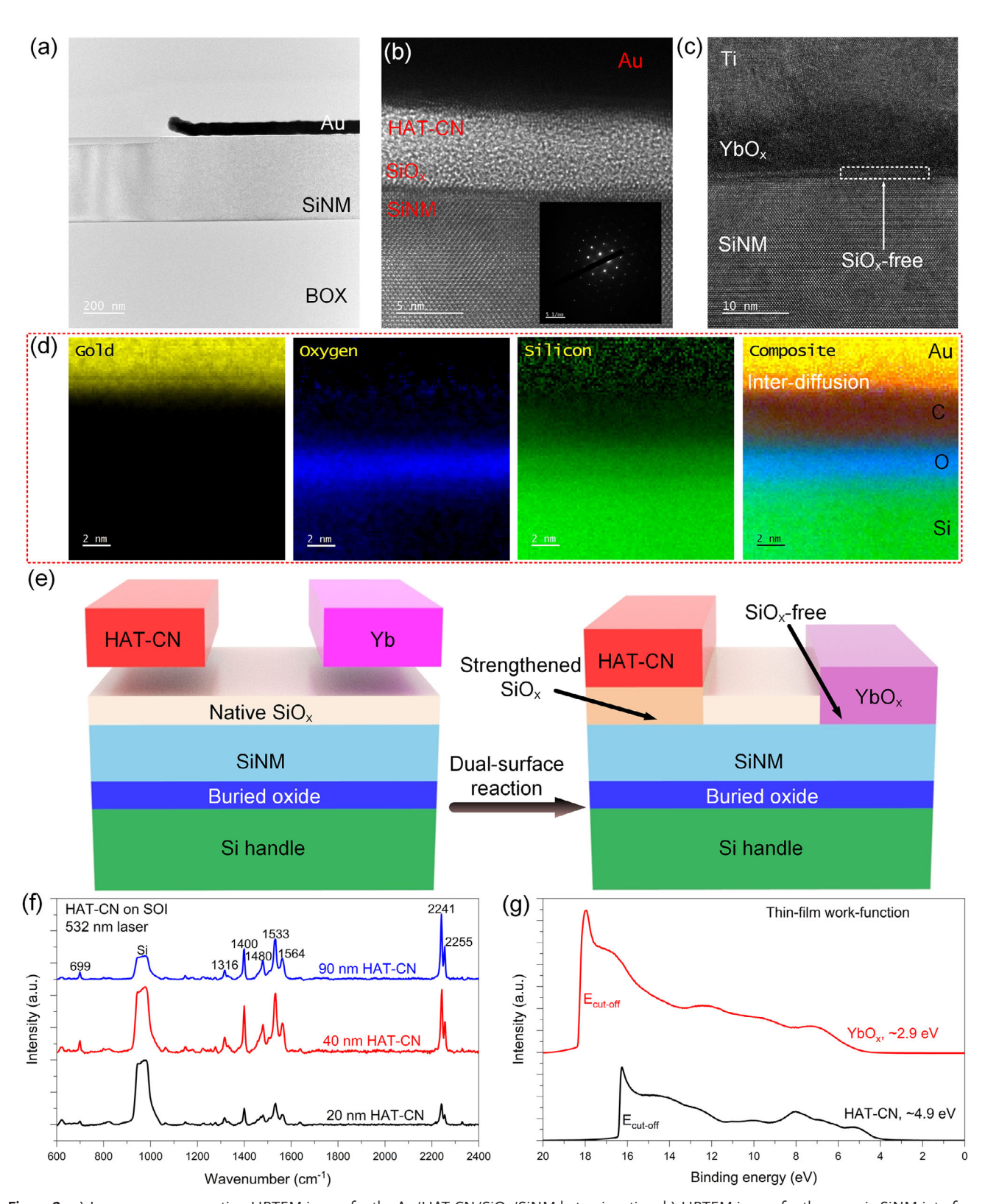


Figure 2. a) Large area cross section HRTEM image for the Au/HAT-CN/SiO $_x$ /SiNM heterojunction. b) HRTEM image for the organic-SiNM interface, with an inset showing the lattice diffraction pattern. c) HRTEM image for Ti/YbO $_x$ /SiNM interface, implying the eliminated SiO $_x$ due to reaction. d) EELS mapping results for organic-SiNM interface, indicating the presence of SiO $_x$, and the inter-diffusion between Au and HAT-CN. e) Indication of the dual-surface reaction process, for which the Yb reacts to eliminate the SiO $_x$, and HAT-CN reacts to further strengthen the SiO $_x$. f) Raman spectra for HAT-CN thin films deposited on SOI substrate with different HAT-CN thicknesses. g) UPS results for both YbO $_x$ and HAT-CN thin films with 20 nm thickness.





www.afm-journal.de

HAT-CN, resulting in an overlap interdiffusion region. The native SiO_x grown at room temperature was of low quality. The native SiO, layer was further strengthened by high-energy HAT-CN particles (by evaporation) approaching the surface. This dualsurface reaction process is illustrated in Figure 2e, where the Ohmic contact surface is optimized by Yb reacting with the initial native SiO_v to achieve low-resistance contact (as shown in Figure 2c), and HAT-CN reacting with the surface to further strengthen the SiOx, thereby passivating the surface and creating a high Schottky barrier. The surface reaction and bonding process between HAT-CN and SiO_x are illustrated in Figure S7 (Supporting Information). The mechanism is described somewhere else, [49] and will be confirmed below. The entire process provides a facile and effective method to realize ultra-high performance organic-inorganic heterojunctions. The Raman spectra (532 nm excitation laser) for varying samples are shown in Figure S8 (Supporting Information), revealing the presence of SiO_v. An increased Si-O bond ratio from HAT-CN on SOI samples (Table S1, Supporting Information) further confirms the reaction between HAT-CN and SiO_v.

Figure 2f illustrates the Raman spectra from 600 to 2400 cm⁻¹ (532 nm excitation laser) for HAT-CN thin films deposited on an SOI substrate. The measurements include three HAT-CN film thicknesses: \approx 90, \approx 40, and \approx 20 nm. Distinct vibrational modes are observed at several labelled peaks, originating from both the underlying silicon substrate and HAT-CN layer. The broad peak at ≈965 cm⁻¹, spanning 900–1030 cm⁻¹, is attributed to second-order Raman scattering from the silicon substrate. The Raman shift at ≈699 cm⁻¹ corresponds to specific vibrational modes of the central aromatic ring, while peaks at ≈ 1400 , ≈ 1480 , and ≈1533 cm⁻¹ are associated with various stretching vibrations within the aromatic ring system. [50] The bands at \approx 2241 and ≈2255 cm⁻¹ are related to the C≡N bond and nitrile vibrations, respectively.[50-52] The Raman spectra of HAT-CN powder are given in Figure S9 (Supporting Information), with different measurement spots. The Raman spectra for HAT-CN thin-film measured by another 785 nm excitation laser are presented in Figure \$10 (Supporting Information). The work function of the HAT-CN and YbOx is determined by ultraviolet photoelectron spectroscopy (UPS) in Figure 2g. A \approx 2 eV cut-off energy ($E_{\text{cut-off}}$) difference is exhibited between the two materials; work-functions of \approx 4.9 and \approx 2.9 eV are respectively obtained for HAT-CN and YbO_v, implying a large energy level tunability of the two contact buffer layers. The high work-function of HAT-CN generates a large upward energy band bending with electron-rich SiNM (4.05 eV electron energy affinity). Ideally, the HAT-CN is expected to form a ≈0.85 eV Schottky barrier height between n-Si, calculated from the difference between the HAT-CN work-function and the n-Si electron affinity. However, the practical Schottky barrier height may not approach this value due to the presence of surface states, which trap the electric charges and hinder the potential drop between two contact materials. As such, the native SiO_x at the interface provides sufficient chemical passivation effect to saturate the surface states and thus generate a high barrier height exceeding ≈0.8 eV (as simulated below).

The elemental composition at the organic-SiNM interface is further revealed in **Figure 3**. The time of flight secondary ion mass spectroscopy (ToF-SIMS) results of the Au/HAT-CN/SiO $_{\rm x}$ /SiNM hetero-interface are presented in Figure 3a,

where the elemental intensity is plotted as a function of sputter time for CN, Si, Au, O and SiO ions. Cyanide ions are selected to specify the presence of HAT-CN. Before ≈200 s sputter time. Au is the primary element as expected. The Au signal drops at \approx 200 s, where the CN signal rises, denoting the interface at Au/HAT-CN. The oxygen signal emerges at the point when the CN signal reaches its maximum value, approximately at 215 s. The major source of oxygen is silicon native oxide, and a small amount of oxidized nitride from HAT-CN also accounts for the observed oxygen, as discussed in the X-ray photoelectron spectroscopy (XPS) analysis below. The O and SiO signals reach their highest values before the CN signal drops, evoking a mixture of the interface between HAT-CN and SiO_v. Figure 3b displays the XPS spectra for the overall elements from 0 to 600 eV binding energy (B. E.) at a depth of 16 (which is within the HAT-CN layer). A mixture interface with peaks dominated by Au, oxygen, nitrogen, carbon, and Si is observed. Standard fingerprint peaks for N 1s (Figure 3c) and Si 2p (Figure 3d) are presented at varying etch depths to further investigate the interface. In Figure 3c, the N signal appears at a depth of 14 and almost disappears, with weak intensity, at a depth of 20. A peak B. E. shift is noticed from depth 16 to 20. The lower B. E. peak of Si-N (≈397.4 eV) emerges as the etch depth increases. [53,54] Similar observations have been reported when the silicon surface reacts with N-containing organics. [53–55] The presence of SiO_v is disclosed in Figure 3d. At depths 15 and 16, prominent SiO_x peaks are observed at \approx 100.1 and \approx 102.6 eV, while these peaks vanish at higher depths of 19 and 20 when approaching the single-crystal Si lattice. Au 4f peaks are fitted in Figure 3e, consisting of two prominent peaks: bulk Au $4f_{7/2}$ at \approx 84 eV and bulk Au 4f_{5/2} at \approx 87.7 eV.^[56] Peak fitting for Si 2p in Figure 3f further reveals the condition of silicon oxide at depth 16. Two sharp peaks at B. E. of \approx 100.1 and \approx 99.4 eV are typical Si $2p_{1/2}$ and Si $2p_{3/2}$ signals.^[57,58] The broad peak at \approx 100.1 eV corresponds to Si–O–C bonding.^[59] The broad peak at ≈102.6 eV corresponds to Si 2p from carbon-bonded SiO_x, as reported.^[58,60] These results further confirm the surface reaction process as suggested in Figure 2e and Figure S7 (Supporting Information). The N 1s XPS spectrum in Figure 3g consists of two prominent peaks, which account for two types of nitrogen atoms in HAT-CN: pyridinic N at ≈398.4 eV and nitrile N at ≈400.2 eV.[61,62] Similar to the observation from previous literature, small parts of nitrogen atoms bond with oxygen as oxidized N (≈402.8 eV) or alkyl nitrite (≈404.1 eV), and some N atoms break out of HAT-CN and form alkylammonium N at \approx 401.3 eV.^[61] The N 1s peaks at higher etch depth are fitted in Figure S11 (Supporting Information), showing a dominant Si-N bonding: as the depth goes from 16 to 20, the oxidized N and alkyl nitrite signal disappear due to the distinct distance from the surface native SiO_{ν} , which is consistent with the ToF-SIMS diagram after 300s where CN- signal intensity is still higher than that from O- signal. Thermally evaporating HAT-CN to strengthen the SiO, is further confirmed in Figure S12 (Supporting Information). XPS results of the native SiO_x for as-received SOI wafers (without depositing HAT-CN on top) suggest a weak Si-O bonding for the unreacted surface.

2.3. Device Optoelectronic Performance

The optoelectronic properties are measured in **Figure 4**. Figure 4a shows the current-voltage (I-V) curves under dark, with

.com/doi/10.1002/adfm.202516835 by Univ of California

awrence Berkeley National Lab, Wiley Online Library on [16/10/2025]. See the Terms and Conditions (https://onlinelibrary.wiley.

onditions) on Wiley Online Library for rules of use; OA articles are governed by the applicable Creative Commons License

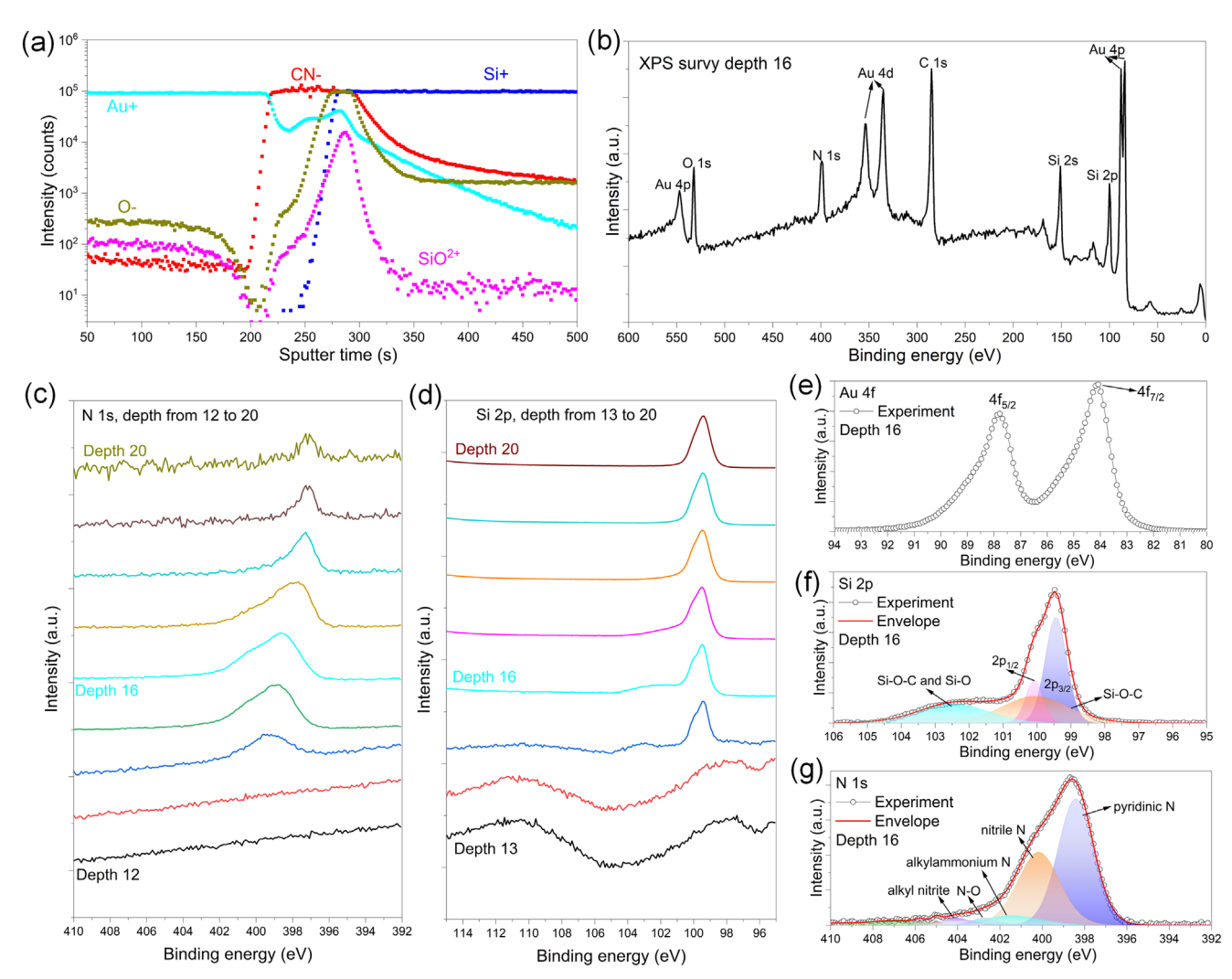


Figure 3. a) TOF-SIMS results for Au/HAT-CN/SiNM. b) XPS results of the overall elemental survey at Au/HAT-CN/SiNM interface. c) N 1s XPS results at different etch depths. d) Si 2p XPS results at different etch depths. e) Au 4f XPS peak fitting at etch depth 16. f) Si 2p XPS peak fitting at etch depth 16. g) N 1s XPS peak fitting at etch depth 16.

exponential (left) and linear (right) scales. A sub-pA/µm level reverse dark current is observed, indicating ultra-low noise. A rectification ratio of $\approx 3 \times 10^7$ is obtained at ± 5 V, resulting from the significant blocking of carrier injection under reverse bias and allowing for a majority carrier injection under forward bias. The Schottky barrier height Φ_{R} is calculated to be ≈ 0.87 eV in Figure \$13 (Supporting Information). [63] This high Schottky barrier height is a result of the high work-function from HAT-CN and the surface chemical passivation from SiO_v. As discussed in Figure 2g, the ≈4.9 eV work function of HAT-CN ideally generates ≈ 0.85 eV Schottky barrier with n-Si, given $\Phi_R = \Phi_m$ – χ_s (where χ_s is the SiNM electron affinity, 4.05 eV). The obtained ≈ 0.87 eV Φ_B agrees with the ideal barrier height, implying the reaction-strengthened SiO_x (Figure 2e) provides significant chemical passivation that overcomes the surface Fermi level pinning effect.^[63] In Figure 4a, under a small forward voltage bias of <230 mV, a voltage shift of below 85 mV is obtained when the current increases one order of magnitude, as calculated in Figure \$14 (Supporting Information). This suggests excellent charge injection capability through the contacts. The reproducibility of this ultra-low reverse dark current is confirmed by several independent measurements in Figure \$15 (Supporting Information), displaying excellent reproducibility of the pA level reverse current. The devices also show highly stable performance over time (Figure \$16, Supporting Information). For devices stored in ambient air for 16 months, tens of pA reverse dark current is still observed. Both organic and interface degradation may lead to device performance degradation, given a stable Si lattice. The contact selection on device performance is discussed in Figure 4b, which explores various contacts proposed in Figure 1c. The Al forms a "high-resistance Ohmic contact" with a low forward current level at 10^{-8} – 10^{-7} A at 3 V. We note that Al is commonly considered to form a slight Schottky barrier with n-Si, and this barrier influences the carrier injection under forward bias. [64] The influence of the metal capsulation layer (as shown in Figure 1c-i,ii) is investigated in Figure 4b. For devices represented by the red and black curves, low-workfunction Ti and high-work-function Au plates were respectively

loi/10.1002/adfm.202516835 by Univ of California

awrence Berkeley National Lab, Wiley Online Library on [16/10/2025]. See the Terms and Conditions (https://

of use; OA articles are governed by the applicable Creative Commons License

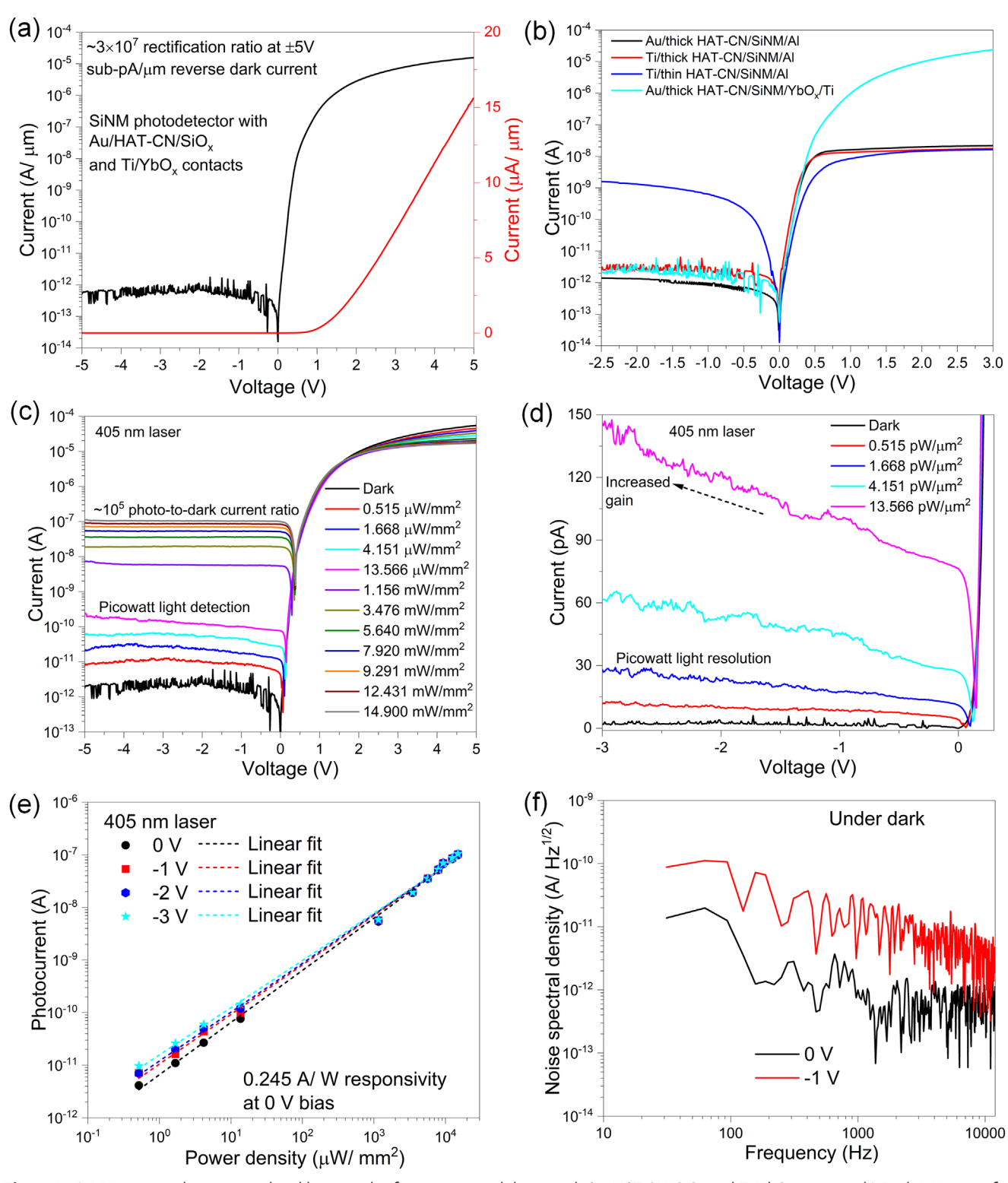


Figure 4. a) *I–V* curves with exponential and linear scales for an optimized device with Au/HAT-CN/SiO_x and Ti/YbO_x contacts. b) Dark *I–V* curves for devices with various contacts. c) Photocurrent-voltage measurements under different illumination power intensities (405 nm laser). d) Linear current-voltage curves under small illumination power. e) Photocurrent as a function of incident power density at varying biases. f) Noise current spectral density.





www.afm-journal.de

deposited on a thick HAT-CN layer (4-6 nm), with both devices having the same HAT-CN thickness. Both devices exhibit similar reverse and forward currents, indicating that the surface barrier height is primarily determined by the nanometer-thin organic buffer layer, rather than the metal capsulation layer. Thin HAT-CN layers (2-4 nm) were deposited with Ti to study the rectification properties, see the blue curve where the reverse current level is increased to the nA scale. This signifies that the contact is transferred into a "high resistance Ohmic contact" due to the lack of conformity of the organic buffer layer, leading to leakage carrier injection from Ti into SiNM. This confirms that the interfacial organic layer, with a thickness of a few nanometers, dominates the entire contact properties, providing a potential method for engineering rectification properties in organic-inorganic heterojunctions. Further, the grain boundary of HAT-CN thin films with varying thicknesses is investigated by AFM in Figure S17 (Supporting Information). For ≈2 and ≈3.3 nm HAT-CN, discontinuous organic islands are formed (Figure S17a,b, Supporting Information). Consequently, the organic-inorganic junctions are transferred to Ohmic contacts in Figure 4b (blue curve). This suggests that the insufficiently conformal organic layer loses its control over the Si surface energy band bending. Thick organic layers with continuous thin films (Figure S17c,d, Supporting Information) are observed to form high-performance rectifying junctions in Figure 4b. These results together indicate that engineering the grain boundary is a promising research direction for multifunctional organic-inorganic optoelectronics. The Ohmic contact is further optimized by replacing Al with Ti/YbO, stacks (cyan curve in Figure 4b), as proposed in Figure 1c-iii. An increase of over three orders of magnitude is obtained for the forward current at 3 V for devices with a Ti/YbO_v contact, compared with that of Al contact devices. This indicates that YbO, dramatically reduces the contact resistance by generating a downward surface band bending for an electron accumulation layer, as suggested in Figure 1b. Photocurrent-voltage curves are measured in Figure 4c under illumination with a 405 nm wavelength laser at various power intensities. The device exhibits a pA-level photocurrent resolution, ranging from several pA (red curve) to hundreds of pA (magenta curve), corresponding to faint pW light illumination on the device area. Under a large optical injection, the device exhibits a photo-to-dark ratio of up to 105, as shown by the gray curve in Figure 4c, where ≈14.9 mW mm⁻² laser power was used. To better understand the photocurrent response, linear-scale *I–V* curves under pW level illumination are plotted in Figure 4d. A distinguished photocurrent is observed at 0 V bias, proving the self-powered mode. Photocurrent increases with a higher reverse bias, indicating the photoconductive gain effect. Namely, the large carrier mobility difference between HAT-CN and YbOx leads to a photocarrier re-cycling effect, in which one electron-hole pair generates more than one photocurrent. [65] Nevertheless, the device demonstrates clear resolution to pW light illumination due to the reduced dark current. The photocurrent versus light intensity at varying biases is plotted in Figure 4e. The devices in this work are photovoltaic-type photodetectors. At 0 V bias, Shockley-Queisser's limit states that the photodiode doesn't exhibit a gain effect. The maximum responsivity corresponds to the case where photocarriers are fully collected. Namely, photo-

recombination loss and no photocarrier recycling. At higher bias, the responsivity ($\approx 0.47 \text{ A W}^{-1}$ at -3 V) exceeds the one-photonone-electron limit (0.33 A W⁻¹ at 405 nm wavelength). [66,67] suggesting that the device exhibits gain due to lifetime and transit time variations between photoelectrons and holes. A high linearity of photocurrent with incident power is displayed in Figure 4e at 0 V bias, meaning that the high organic-inorganic interfacial barrier is sufficient to extract a noteworthy amount of photocarriers without requiring external bias. [66,67] The responsivity is calculated to be ≈ 0.245 A W⁻¹ at 0 V bias. The noise current spectrum is measured in Figure 4f. 10⁻¹² to 10⁻¹¹ A/ Hz^{1/2} noise current density is obtained for the device up to 10 kHz. In Figure 4f, 1/f noise is present at low frequency at both -1 V and 0 V biases. This could be the trapping/de-trapping of carriers by interfaces, or the noise from the test system. Another possibility is that charge injection from the contact region is not fully mitigated for a biased junction. At high frequency, the thermal noise dominates.

Figure 5 investigates the temporal photovoltage response of

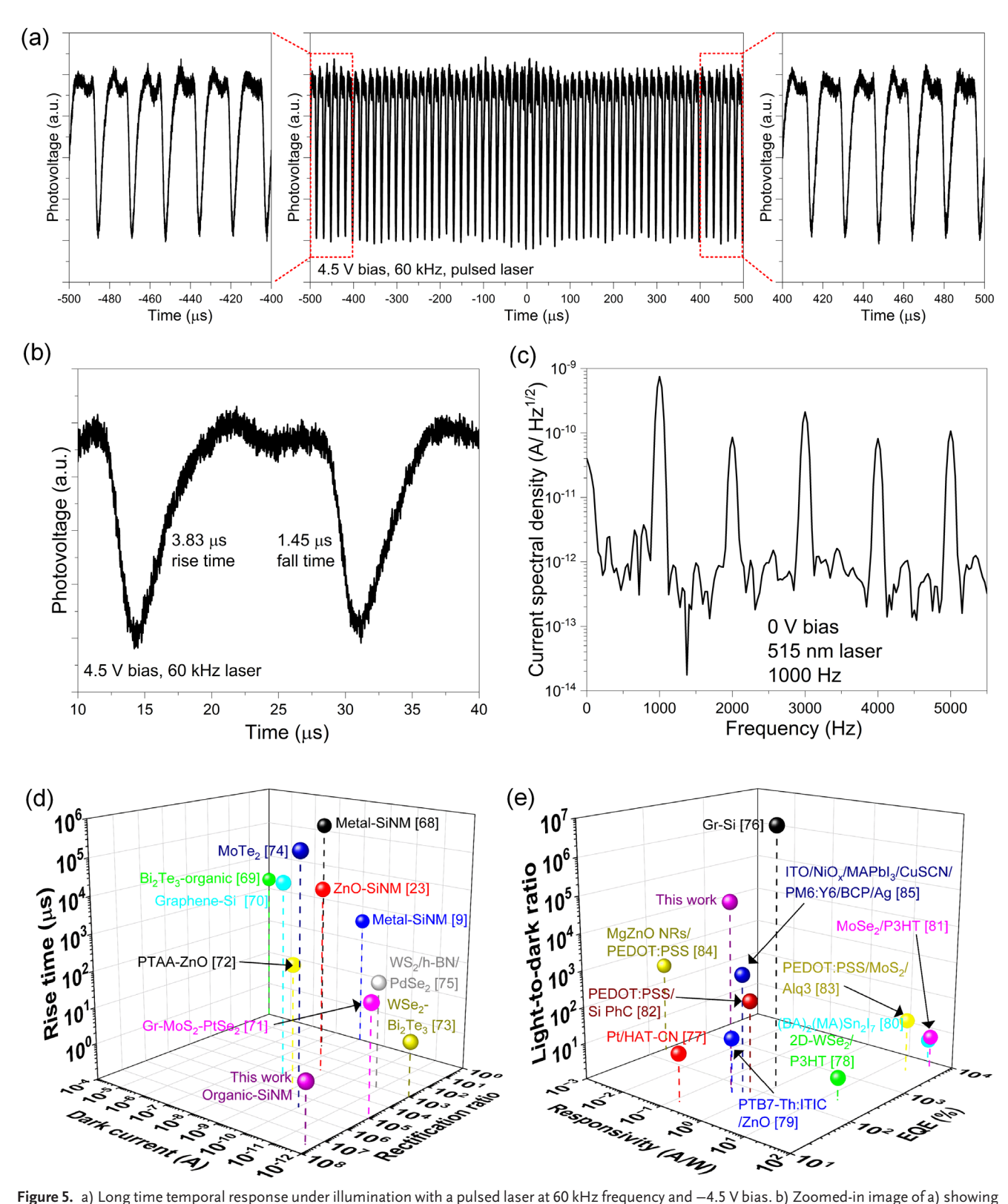
the photodetectors. Figure 5a measures the long time scale (1 ms) response stability under pulsed laser illumination (520 nm, 39 ns pulse width), for which the laser was modulated at 60 kHz. Without additional bias, the photodetector exhibits a stable photovoltage response for self-powered operation (Figure S18, Supporting Information). Figure 5b determines the response speed from the results in Figure 5a. The hybrid device exhibits a typical photovoltaic effect-based response. [66] $\approx 3.83/\approx 1.45~\mu s$ rise/fall times are obtained. The response speed of a photodetector is primarily governed by the carrier transit time and the resistancecapacitance (RC) constant. In this work, the high carrier mobility and confined photocarrier generation volume for SiNM significantly shorten the carrier transit time within the Si layer. Additionally, the small device area and the optimized contact interfaces effectively minimize the RC constant. The use of a moderately thin HAT-CN further alleviates the transit times within the low-mobility organic layer. Collectively, these factors contribute to the microsecond-fast photoresponse. Notably, the speed in this work is practically limited by the mobility in organic layers and the test equipment (for example, the explored pre-amplifier has a response time limit of ≈ 1 µs). The device effectively responds within the Si absorption range. The temporal response was tested using a continuous power 1060 nm laser (Figure S19, Supporting Information), demonstrating the device's capability to detect a broad range of wavelengths. The current spectral density (CSD) under illumination is illustrated in Figure 5c with a 1000 Hz laser frequency and no voltage bias. Significant photocurrent peaks appear at frequencies with an integral order of 1000 Hz, and the device noise level is below 10^{-12} A/Hz^{1/2}. The frequency is plotted as a log-log scale in Figure S20 (Supporting Information). At low frequency, 1/f noise is present, in agreement with that observed in Figure 4f. At high frequency, a constant CSD further confirms that the noise current is dominated by thermal noise. Some key metrics, including dark current, rectification ratio and rise time, are compared between our device and stateof-the-art reports in Figure 5d.[9,23,68-75] Note that there are variations in material natural properties, device area and measurement methods among these reports, and we use "1" rectification ratio for devices with symmetrical contacts. [9,68] It is noted that 2-D material based photodetectors have a comparably low dark current level.[71,73] Organic-inorganic heterojunctions typically

electrons and photoholes are respectively directed to Ti/YbO, and

Au/HAT-CN contacts, and transferred into photocurrent with no

16163028, 0, Downloaded from https://advanced.onlinelibrary.wiley.com/doi/10.1002/adfm.202516835 by Univ of California Lawrence Berkeley National Lab, Wiley Online Library on [1610/2025], See the Terms and Conditions (https://onlinelibrary.wiley.com/doi/10.1002/adfm.202516835 by Univ of California Lawrence Berkeley National Lab, Wiley Online Library on [1610/2025], See the Terms and Conditions (https://onlinelibrary.wiley.com/doi/10.1002/adfm.202516835 by Univ of California Lawrence Berkeley National Lab, Wiley Online Library on [1610/2025], See the Terms and Conditions (https://onlinelibrary.wiley.com/doi/10.1002/adfm.202516835 by Univ of California Lawrence Berkeley National Lab, Wiley Online Library on [1610/2025], See the Terms and Conditions (https://onlinelibrary.wiley.com/doi/10.1002/adfm.202516835 by Univ of California Lawrence Berkeley National Lab, Wiley Online Library on [1610/2025], See the Terms and Conditions (https://onlinelibrary.wiley.com/doi/10.1002/adfm.202516835 by Univ of California Lawrence Berkeley National Lab, Wiley Online Library on [1610/2025], See the Terms and Conditions (https://onlinelibrary.wiley.com/doi/10.1002/adfm.202516835 by Univ of California Lawrence Berkeley National Lab, Wiley Online Library on [1610/2025], See the Terms and Conditions (https://onlinelibrary.wiley.com/doi/10.1002/adfm.202516835 by Univ of California Lawrence Berkeley National Lab, Wiley Online Library on [1610/2025], See the Terms and Conditions (https://onlinelibrary.wiley.com/doi/10.1002/adfm.202516835 by Univ of California Lab, Wiley Online Library on [1610/2025], See the Terms and Conditions (https://onlinelibrary.wiley.com/doi/10.1002/adfm.202516835 by Univ of California Lab, Wiley Online Library on [1610/2025], See the Terms and Conditions (https://onlinelibrary.wiley.com/doi/10.1002/adfm.202516835 by Univ of California Lab, Wiley Online Library on [1610/2025], See the Terms and Conditions (https://onlinelibrary.wiley.com/doi/10.1002/adfm.20251684 by Univ of California Lab, Wiley Online Library on

nditions) on Wiley Online Library for rules of use; OA articles are governed by the applicable Creative Commons License



the shape of photovoltage, and the device's rise/fall time. c) Current spectral density under illumination with a CW laser at 1000 Hz, without applied bias. d) Metric (rise time, dark current and rectification ratio) comparison between this work and the advanced photodetector reports. e) Metric (responsivity, EQE and light-to-dark ratio) comparison between this work and the state-of-the-art photodetectors.



www.afm-journal.de

suffer from the high response time due to the low carrier mobility within organics. [69,72] The demonstrated organic-SiNM photodiodes in this work have a pA level dark current. $\approx 3 \times 10^7$ rectification ratio, and us fast response speed among the metal-SiNM junctions, [9,68] metal oxide-SiNM junction, [23] organic-inorganic heterojunctions, [69,72] 2-D/3-D heterojunctions, [70] and 2-D material photodetectors. [71,73,74] Other performance metrics, including spectral responsivity, light-to-dark current ratio and external quantum efficiency (EQE) of our device, are compared with the state-of-the-art photodetectors in Figure 5e. [76-85] The spectral responsivity is measured at 0 V bias in this work, meaning no photoconductive gain effect. Under an applied voltage bias, other reported photodetectors can possess hundreds of A/W responsivity for devices with a gain effect.^[71] 0.245 A/W responsivity (our device) at 0 V bias is competitively high among the non-gain devices, the upper limit of which is defined by the one-photon-oneelectron condition. [66] The EQE of our devices is ≈75% at 405 nm, close to the 100% EQE limit for a non-gain device. A trade-off exists between the gain effect and the noise level for a photodetector. For example, photodiodes or photoconductors possess high responsivity due to the large variation between the carrier transition time and lifetime, but suffer from high noise current and a low signal-to-noise ratio. [80,81] The $\approx 10^5$ photo-to-dark ratio for our device is also comparable to those from bulk semiconductor devices, [12,65,76,82] which have a high optical absorption rate. The test conditions, such as the use of a defocused laser beam, also limit the light-to-dark current ratio in this work. In addition to those organic-inorganic heterojunctions with bulk semiconductors, microsecond-fast response and high detectivity have been reported in 2D material-based photodetectors.^[86] Our devices also demonstrate a comparatively low NEP at a 10⁻¹¹ W/Hz^{1/2} level and an ultra-high rectification ratio compared with emerging 2D material photodetectors.[86] In summary, the advanced performance metrics in this work suggest that tailoring dualinterface reactions is an effective strategy for nanomembrane optoelectronic devices.

2.4. Imaging System

The proposed interfacial strategies, along with the resulting high device performance and large-area device uniformity, further advance the systemic applications of our organic-inorganic heterojunctions. An imaging system is demonstrated in Figure 6. In Figure 6a, a white LED illuminates a shadow mask (mounted on a movable stage), and the transmitted light is focused on the photodiodes, which are wire-bonded to a testing board (Figure 6b). The output of the photodiodes is connected to a multiplexer (MUX), whose signal is then amplified by a pre-amplifier. A micro-controller is utilized for the sampling circuit, which selects signals from different photodiodes, and a computer records the measured photocurrent. Spatially resolved photocurrent data from different regions of the mask are collected by moving the stage along one direction. No bias was applied for the photodiodes during the imaging process. 19 random measurements were conducted over the chip area to show the uniformity of the reverse dark current (Figure 6c, where the dark current distribution is plotted with voltage). Most of the dark currents are distributed at the pA level, confirming the potential of our device

strategy for application in large-area commercial imaging systems. The I-V curves and reverse current data point distribution for the 19 measurements are given in Figure S21 (Supporting Information). The imaging results shown in Figure 6d reveal a clear distinction between photocurrent in the mask's open region ("CAL") and dark current in the fully shadowed region. 56×33 pixels are indicated for the image. Surface passivation of the photodiode enhances responsivity without additional bias, as suggested in Figure 4e, enabling low-power operation. As a result, a distinct photocurrent is obtained without external power applied to the photodiode array, demonstrating a self-powered imaging system. The resolution of the imaging results can be further enhanced by improving the test system. In summary, the demonstrated interface reaction-based strategies show great potential for both device- and system-level applications in organicinorganic heterojunctions.

3. Conclusion

This work demonstrates the ultra-high performance of an organic-SiNM photodetector. Nanometer-thin HAT-CN is integrated with the SiO_v/SiNM interface, resulting in a high surface Schottky height due to the high organic work function and surface chemical passivation properties. The dark current is further mitigated by blocking the hole injection current on the Ohmic contact side through the insertion of an emerging material YbO_v. The contact selection and its influence on device performance are thoroughly investigated and discussed to demonstrate the universality of the proposed mechanism and observed results. The optimized devices exhibit pA-level low dark current noise, a rectification ratio of over 10⁷, us response speed, and self-powered photodetection, placing these devices among the highest-performing reported photodetectors. A self-powered imager utilizing devices with the proposed interfacial strategies is demonstrated, indicating the great potential of this organic-inorganic heterojunction in systems requiring low-power consumption. The reported insights are expected to propel the development of high-performance organic/silicon nanomembrane heterojunctions, with further contact optimization through the engineering of interfacial materials.

4. Experimental Section

Device Fabrication and Characterization: The devices were fabricated from commercial SOI wafers (400 and 55 nm device layer thickness, <100> orientation, electron-rich). Photolithography and subsequent RIE processes were employed to define the device area. Two additional photolithography steps were used to define the contact region. The contacts were then deposited to finish the device fabrication after the lift-off process. A thermal evaporator was used to deposit the organic contact. The deposition rate was optimized at $\approx\!0.3$ Å s $^{-1}.$ An e-beam evaporator was used to deposit Al, Ti, and Yb contacts at deposition rates of ≈ 1 , ≈ 1.1 , and $\approx 1.1 \text{ Å s}^{-1}$, respectively. A sputtering system was used to deposit Au at $\approx\!1.1~\mbox{\normalfon}\mbox{\normalfon}$ A Bruker Dimension Icon AFM was used to take the AFM images. The Raman shifts were acquired by an Invia Raman spectrometer. The Raman spectra were baseline-corrected, averaged from five distinct spots per sample, and normalized. A Thermo Fisher Scientific UPS was explored to measure the work functions. The HRTEM and EELS results were taken by a JEOL F200 S/TEM. The XPS results were taken

16163028, 0, Downloaded from https://advanced.onlinelibrary.wiley.com/doi/10.1002/adfm.202516835 by Univ of California

awrence Berkeley National Lab, Wiley Online Library on [16/10/2025]. See the Terms and Conditions (https://onlinelibrary.wiley.

on Wiley Online Library for rules of use; OA articles are governed by the applicable Creative Commons

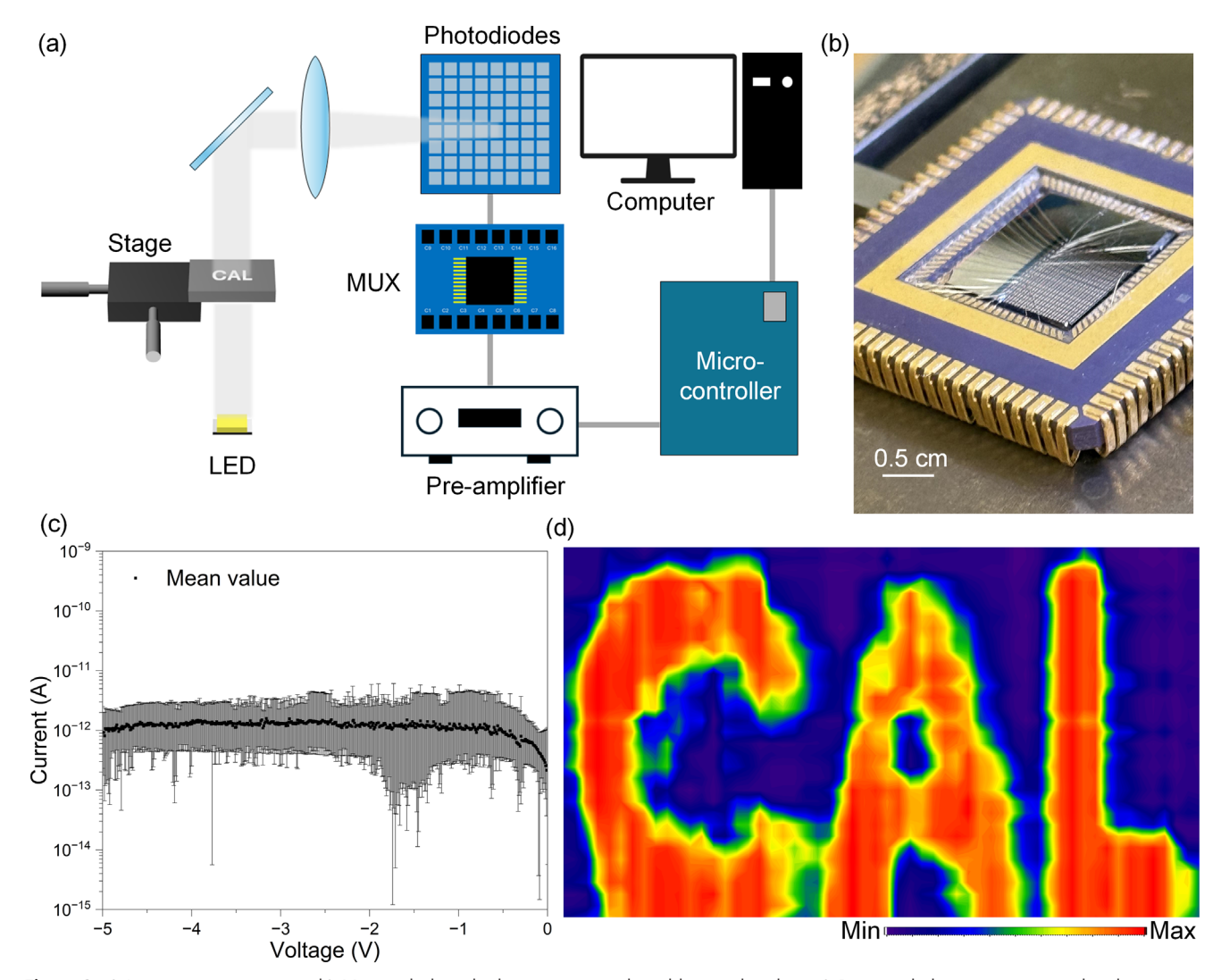


Figure 6. a) Imaging system set-up. b) Mounted photodiodes on a testing board by wire-bonding. c) Reverse dark current statistic distribution as a function of voltage, for 19 random tests. d) Imaging results using a "CAL" shadow mask. Photocurrent is the metric reflecting the "CAL" image.

by a Thermo Fisher Scientific K-Alpha XPS. Current-voltage (*I–V*) curves were measured by a Keithley 4200 semiconductor analyzer at room temperature. A continuous power (CW) fiber-coupled laser from Thorlabs (LP405-SF10) illuminated the device area for photocurrent-voltage measurements. For temporal response measurement, both CW laser (Thorlabs, LP515-SF3) and pulsed laser (Thorlabs, NPL52B with 39 ns pulse width) were used to illuminate the device. A function generator modulated the laser frequency/repetition rate. The output photovoltage signal from the device was connected to a current pre-amplifier (Stanford Research SR570).

Statistical Analysis: All experiments were conducted for more than 3 times to confirm the reproducibility of the results. The AFM results were analyzed by a software NanoScope Analysis. The XPS data baseline subtraction and peak fitting in Figure 3f,g and Figure S11 (Supporting Information) were conducted using a software Thermo Advantage. The XPS results in Figure 3c,d and Raman results in Figure 2f and S9,S10 were normalized. The raw Raman spectra were processed by cosmic ray removal and baseline subtraction in Python. In Figure 6c, I–V measurements were conducted for 19 times and got the average/maximum/minimum dark current as a function of voltage. All the rest of results were shown as directly measured from the instruments.

Supporting Information

Supporting Information is available from the Wiley Online Library or from the author.

Acknowledgements

Y.Z., G.V., and H.W. contributed equally to this work. This work was supported by the Ontario Research Foundation – Research Excellence program, the Natural Sciences and Engineering Research Council of Canada, and the University of Toronto. The authors thank Sandra Gibson (Quantum-Nano Fabrication and Characterization Facility, QNFCF) for assistance with the AFM characterization. The authors thank Nicki Shaw (QNFCF) for assistance with FIB/TEM. The authors also acknowledge Peter Brodersen (Ontario Centre for the Characterization of Advanced Materials, OCCAM) for assistance with the UPS, XPS, and TOF-SIMS characterizations.

Conflict of Interest

The authors declare no conflict of interest.

16163028, 0, Downloaded from https://advanced.onlinelibrary.wiley.com/doi/10.1002/adfm.202516835 by Univ of California

Berkeley National Lab, Wiley Online Library on [16/10/2025]. See the Terms and Conditions (https://onlinelibrary.wiley.

on Wiley Online Library for rules of use; OA articles are governed by the applicable Creative Commons



Data Availability Statement

The data that support the findings of this study are available from the corresponding author upon reasonable request.

Keywords

dual-surface reaction, faint light detection, high work-function organics, organic-inorganic photodetectors, self-powered imaging

Received: July 1, 2025 Revised: August 18, 2025 Published online:

- [1] J. A. Rogers, T. Someya, Y. Huang, Science 2010, 327, 1603.
- [2] Z. Hu, H. Guo, D. An, M. Wu, A. Kaura, H. Oh, Y. Wang, M. Zhao, S. Li, Q. Yang, X. Ji, S. Li, B. Wang, D. Yoo, P. Tran, N. Ghoreishi-Haack, Y. Kozorovitskiy, Y. Huang, R. Li, J. A. Rogers, Adv. Mater. 2024, 36, 2309421.
- [3] M. Faghih, D. Karnaushenko, Q. A. Besford, C. Becker, R. Ravishankar, D. D. Karnaushenko, G. Cuniberti, A. Fery, O. G. Schmidt, Adv. Funct. Mater. 2022, 32, 2200233.
- [4] J. A. Rogers, M. G. Lagally, R. G. Nuzzo, Nature 2011, 477, 45.
- [5] P. Zhang, E. Tevaarwerk, B. N. Park, D. E. Savage, G. K. Celler, I. Knezevic, P. G. Evans, M. A. Eriksson, M. G. Lagally, *Nature* 2006, 439-703
- [6] M. M. Roberts, L. J. Klein, D. E. Savage, K. A. Slinker, M. Friesen, G. Celler, M. A. Eriksson, M. G. Lagally, Nat. Mater. 2006, 5, 388.
- [7] G. Li, Z. Ma, C. You, G. Huang, E. Song, R. Pan, H. Zhu, J. Xin, B. Xu, T. Lee, Z. An, Z. Di, Y. Mei, Sci. Adv. 2020, 6, aaz6511.
- [8] A. K. Katiyar, B. J. Kim, G. Lee, Y. Kim, J. S. Kim, J. M. Kim, S. Nam, J. Lee, H. Kim, J.-H. Ahn, Sci. Adv. 2024, 10, adg7200.
- [9] B. Wu, Z. Zhang, Z. Zheng, T. Cai, C. You, C. Liu, X. Li, Y. Wang, J. Wang, H. Li, E. Song, J. Cui, G. Huang, Y. Mei, Adv. Mater. 2023, 35, 2306715.
- [10] Z. Xia, H. Song, M. Kim, M. Zhou, T. H. Chang, D. Liu, X. Yin, K. Xiong, H. Mi, X. Wang, F. Xia, Sci. Adv. 2017, 3, 1602783.
- [11] J. H. Seo, K. Zhang, M. Kim, D. Zhao, H. Yang, W. Zhou, Z. Ma, Adv. Opt. Mater. 2016, 4, 120.
- [12] M. Kim, S. Yi, J. D. Kim, X. Yin, J. Li, J. Bong, D. Liu, S. C. Liu, A. Kvit, W. Zhou, X. Wang, Z. Yu, Z. Ma, X. Li, ACS Nano 2018, 12, 6748.
- [13] G. Li, E. Song, G. Huang, R. Pan, Q. Guo, F. Ma, B. Zhou, Z. Di, Y. Mei, Small 2018, 14, 1802985.
- [14] P. Feng, I. Monch, G. Huang, S. Harazim, E. J. Smith, Y. Mei, O. G. Schmidt, Adv. Mater. 2010, 22, 3667.
- [15] P. Gutruf, V. Krishnamurthi, A. Vázquez-Guardado, Z. Xie, A. Banks, C.-J. Su, Y. Xu, C. R. Haney, E. A. Waters, I. Kandela, S. R. Krishnan, T. Ray, J. P. Leshock, Y. Huang, D. Chanda, J. A. Rogers, *Nat. Electron.* 2018, 1, 652
- [16] L. Lu, P. Gutruf, L. Xia, D. L. Bhatti, X. Wang, A. Vazquez-Guardado, X. Ning, X. Shen, T. Sang, R. Ma, G. Pakeltis, G. Sobczak, H. Zhang, D. O. Seo, M. Xue, L. Yin, D. Chanda, X. Sheng, M. R. Bruchas, J. A. Rogers, Proc. Natl. Acad. Sci. USA 2018, 115, E1374.
- [17] W. Bai, H. Yang, Y. Ma, H. Chen, J. Shin, Y. Liu, Q. Yang, I. Kandela, Z. Liu, S. K. Kang, C. Wei, C. R. Haney, A. Brikha, X. Ge, X. Feng, P. V. Braun, Y. Huang, W. Zhou, J. A. Rogers, Adv. Mater. 2018, 30, 1801584.
- [18] H. Yang, D. Zhao, S. Chuwongin, J.-H. Seo, W. Yang, Y. Shuai, J. Berggren, M. Hammar, Z. Ma, W. Zhou, Nat. Photon. 2012, 6, 615.
- [19] W. Bai, J. Shin, R. Fu, I. Kandela, D. Lu, X. Ni, Y. Park, Z. Liu, T. Hang, D. Wu, Y. Liu, C. R. Haney, I. Stepien, Q. Yang, J. Zhao, K. R. Nandoliya, H. Zhang, X. Sheng, L. Yin, K. MacRenaris, A. Brikha,

- F. Aird, M. Pezhouh, J. Hornick, W. Zhou, J. A. Rogers, *Nat. Biomed. Eng.* **2019**, *3*, 644.
- [20] M. Medina-Sanchez, B. Ibarlucea, N. Perez, D. D. Karnaushenko, S. M. Weiz, L. Baraban, G. Cuniberti, O. G. Schmidt, *Nano Lett.* 2016, 16, 4288.
- [21] H. C. Ko, M. P. Stoykovich, J. Song, V. Malyarchuk, W. M. Choi, C. J. Yu, J. B. Geddes 3rd, J. Xiao, S. Wang, Y. Huang, J. A. Rogers, *Nature* 2008, 454, 748.
- [22] K. Zhang, Y. H. Jung, S. Mikael, J. H. Seo, M. Kim, H. Mi, H. Zhou, Z. Xia, W. Zhou, S. Gong, Z. Ma, Nat. Commun. 2017, 8, 1782.
- [23] S. Lim, D.-S. Um, M. Ha, Q. Zhang, Y. Lee, Y. Lin, Z. Fan, H. Ko, Nano Res. 2016, 10, 22.
- [24] H. Jang, W. Lee, S. M. Won, S. Y. Ryu, D. Lee, J. B. Koo, S. D. Ahn, C. W. Yang, M. H. Jo, J. H. Cho, J. A. Rogers, J. H. Ahn, *Nano Lett.* 2013, 13, 5600.
- [25] T. Das, H. Jang, J. Bok Lee, H. Chu, S. Dae Kim, J.-H. Ahn, 2D Mater. 2015, 2, 044006.
- [26] Y. Wang, L. Yin, S. Huang, R. Xiao, Y. Zhang, D. Li, X. Pi, D. Yang, Nano Lett. 2023, 23, 8460.
- [27] L. Yin, W. Huang, R. Xiao, W. Peng, Y. Zhu, Y. Zhang, X. Pi, D. Yang, Nano Lett. 2020, 20, 3378.
- [28] N. Zhang, K. Liu, H. Song, Z. Liu, D. Ji, X. Zeng, S. Jiang, Q. Gan, Appl. Phys. Lett. 2014, 104, 203112.
- [29] H. Song, L. Guo, Z. Liu, K. Liu, X. Zeng, D. Ji, N. Zhang, H. Hu, S. Jiang, Q. Gan, Adv. Mater. 2014, 26, 2737.
- [30] R. Pan, Q. Guo, G. Li, E. Song, G. Huang, Z. An, Z. Di, Y. Mei, ACS Appl. Mater. Interfaces 2018, 10, 41497.
- [31] J. Bardeen, Phys. Rev. 1947, 71, 717.
- [32] B. L. Sharma, Metal-Semiconductor Schottky Barrier Junctions and Their Applications, Springer, New York 1984.
- [33] S. Ashok, J. M. Borrego, R. J. Gutmann, Solid-State Electron. 1979, 22, 621
- [34] J.-X. Man, J.-T. Hu, D.-K. Wang, S.-J. He, Z.-H. Lu, Appl. Phys. Lett. 2022, 120, 121101.
- [35] C. Fuentes-Hernandez, W. F. Chou, T. M. Khan, L. Diniz, J. Lukens, F. A. Larrain, V. A. Rodriguez-Toro, B. Kippelen, Science 2020, 370, 698.
- [36] Q. Gan, F. J. Bartoli, Z. H. Kafafi, Adv. Mater. 2013, 25, 2385.
- [37] I. Kymissis, Organic Field Effect Transistors: Theory, Fabrication and Characterization, Springer, New York 2009.
- [38] C. Zhao, J. Park, S. E. Root, Z. Bao, Nat. Rev. Bioeng. 2024, 2, 671.
- [39] Y. Zhou, Optoelectronic Organic-Inorganic Semiconductor Heterojunctions, CRC Press, Boca Raton 2021.
- [40] X. Deng, Z. Li, H. Liu, Y. Zhao, L. Zheng, X. Shi, L. Wang, X. Fang, H. Zheng, Small 2021, 17, 2101674.
- [41] S.-S. Yoon, D.-Y. Khang, Adv. Energy Mater. 2018, 8, 1702655.
- [42] J. He, P. Gao, Z. Ling, L. Ding, Z. Yang, J. Ye, Y. Cui, ACS Nano 2016, 10, 11525.
- [43] Z. Liang, P. Zeng, P. Liu, C. Zhao, W. Xie, W. Mai, ACS Appl. Mater. Interfaces 2016, 8, 19158.
- [44] J.-H. Seo, T.-Y. Oh, J. Park, W. Zhou, B.-K. Ju, Z. Ma, Adv. Funct. Mater. 2013, 23, 3398.
- [45] C. C. Bof Bufon, J. D. Arias Espinoza, D. J. Thurmer, M. Bauer, C. Deneke, U. Zschieschang, H. Klauk, O. G. Schmidt, *Nano Lett.* 2011, 11, 3727.
- [46] H. Zhao, X. Guo, Y. Wang, W. Wang, S. Li, Q. Zhou, T. Zhou, Y. Xie, Y. Yu, F. Xuan, Z. Ni, L. Gao, Laser Photonics Rev. 2024, 18, 2400192.
- [47] F. Cui, V. Garcia-Lopez, Z. Wang, Z. Luo, D. He, X. Feng, R. Dong, X. Wang, Chem. Rev. 2024, 125, 445.
- [48] P. Chen, Y. Xiao, J. Hu, S. Li, D. Luo, R. Su, P. Caprioglio, P. Kaienburg, X. Jia, N. Chen, J. Wu, Y. Sui, P. Tang, H. Yan, T. Huang, M. Yu, Q. Li, L. Zhao, C. H. Hou, Y. W. You, J. J. Shyue, D. Wang, X. Li, Q. Zhao, Q. Gong, Z. H. Lu, H. J. Snaith, R. Zhu, Nature 2024, 625, 516.
- [49] F. E. Ruttenberg, M. J. D. Low, J. Am. Ceram. Soc. 1973, 56, 241.

ADVANCED SCIENCE NEWS

www.advancedsciencenews.com www.afm-journal.de

- [50] W. Pickhardt, M. Wohlgemuth, S. Grätz, L. BorchardJ, Org. Chem. 2021, 86, 14011.
- [51] J. L. Segura, R. Juárez, M. Ramos, C. Seoane, Chem. Soc. Rev. 2015, 44, 6850.
- [52] S. Liu, M. Liu, X. Li, S. Yang, Q. Miao, Q. Xu, G. Zeng, Carbon Energy 2023. 5. 303.
- [53] J. L. Bischoff, F. Lutz, D. Bolmont, L. Kubler, Surf. Sci. 1991, 251, 170.
- [54] A. Pélisson-Schecker, H. J. Hug, J. Patscheider, Surf. Interface Anal. 2012. 44. 29.
- [55] J. Zhao, F. Gao, S. P. Pujari, H. Zuilhof, A. V. Teplyakov, *Langmuir* 2017, 33, 10792.
- [56] S. W. Ong, B. L. Ong, E. S. Tok, Appl. Surf. Sci. 2019, 488, 753.
- [57] A. Montesdeoca-Santana, E. Jiménez-Rodríguez, N. Marrero, B. González-Díaz, D. Borchert, R. Guerrero-Lemus, Nucl. Instr. Meth. Phys. Res. B 2010, 268, 374.
- [58] C. H. D. V. Xavier Wallart, P. Allongue, J. Am. Chem. Soc. 2005, 127,
- [59] S. Ortaboy, J. P. Alper, F. Rossi, G. Bertoni, G. Salviati, C. Carraro, R. Maboudian, Energy Environ. Sci. 2017, 10, 1505.
- [60] Y. L. hung, S. H. Ngalim, A. Scaccabarozzi, D. Narducci, Beilstein J. Nanotechnol. 2015, 6, 19.
- [61] R. Yan, E. Josef, H. Huang, K. Leus, M. Niederberger, J. P. Hofmann, R. Walczak, M. Antonietti, M. Oschatz, Adv. Funct. Mater. 2019, 29, 1902858
- [62] R. J. J. Jansen, H. Van Bekkum, Carbon 1995, 33, 1021.
- [63] Y. Zhang, S. Almenabawy, N. P. Kherani, Sci. Adv. 2023, 9, adg2454.
- [64] T. G. Allen, J. Bullock, X. Yang, A. Javey, S. De Wolf, Nat. Energy 2019, 4, 914
- [65] Y. Zhang, J. Y. Y. Loh, A. G. Flood, C. Mao, G. Sharma, N. P. Kherani, Adv. Funct. Mater. 2022, 32, 2109794.
- [66] Y. Zhang, J. Y. Y. Loh, N. P. Kherani, Adv. Sci. 2022, 9, 2203234.
- [67] M. A. Juntunen, J. Heinonen, V. Vähänissi, P. Repo, D. Valluru, H. Savin, Nat. Photon. 2016, 10, 777.
- [68] H. J. Ha, B. H. Kang, S. W. Yeom, J. Park, Y. H. Lee, B. K. Ju, Nanotechnology 2015, 26, 485501.
- [69] M. Yang, J. Wang, Y. Zhao, L. He, C. Ji, X. Liu, H. Zhou, Z. Wu, X. Wang, Y. Jiang, ACS Nano 2018, 13, 755.

- [70] J. Yin, L. Liu, Y. Zang, A. Ying, W. Hui, S. Jiang, C. Zhang, T. Yang, Y. L. Chueh, J. Li, J. Kang, Light Sci. Appl. 2021, 10, 113.
- [71] J. Y. Wu, H. Y. Jiang, Z. Y. Wen, C. R. Wang, T. Zhang, ACS Appl. Mater. Interfaces 2024, 16, 32357.
- [72] H. J. Ha, S. J. Kang, J. H. Jeong, J. H. Ma, M. H. Park, W. Kim, A. Ha, S. Kim, S. Park, S. J. Kang, ACS Appl. Mater. Interfaces 2024, 16, 40139.
- [73] D. Guo, Q. Fu, G. Zhang, Y. Cui, K. Liu, X. Zhang, Y. Yu, W. Zhao, T. Zheng, H. Long, P. Zeng, X. Han, J. Zhou, K. Xin, T. Gu, W. Wang, Q. Zhang, Z. Hu, J. Zhang, Q. Chen, Z. Wei, B. Zhao, J. Lu, Z. Ni, Adv. Mater. 2024, 36, 2400060.
- [74] M. Rabeel, H. Kim, M. A. Khan, M. Abubakr, I. Ahmad, M. Ahmad, S. Rehman, M.-J. Lee, M. F. Khan, D.-K. Kim, ACS Photonics 2023, 10, 4425.
- [75] Y. Chen, Y. Wang, Z. Wang, Y. Ye, X. Chai, J. Ye, Y. Chen, R. Xie, Y. Zhou, Z. Hu, Q. Li, L. Zhang, F. Wang, P. Wang, J. Miao, J. Wang, X. Chen, W. Lu, P. Zhou, W. Hu, Nat. Electron. 2021, 4, 357.
- [76] P. Ji, S. Yang, Y. Wang, K. Li, Y. Wang, H. Suo, Y. T. Woldu, X. Wang, F. Wang, L. Zhang, Z. Jiang, Microsyst. Nanoeng. 2022, 8, 9.
- [77] Y. Jin, H. S. Kim, J. Park, S. Yoo, K. Yu, ACS Photonics 2021, 8, 2618.
- [78] P. D. Khanikar, S. Dewan, J. W. John, A. Shukla, P. Das, S. Dhara, S. Karak, S.-C. Lo, E. B. Namdas, S. Das, Adv. Electron. Mater. 2023, 9, 2300514
- [79] S. Wang, M. Zhao, D. Jiang, Q. Liang, J. Phys. Chem. Lett. 2025, 16, 5449.
- [80] Y. Xu, F. Wang, J. Xu, X. Lv, G. Zhao, Z. Sun, Z. Xie, S. Zhu, Opt. Express. 2023, 31, 8428.
- [81] P. D. Khanikar, H. K. Sandhu, S. Sharma, S.-C. Lo, E. B. Namdas, S. Das, Adv. Mater. Technol. 2025, 10, 2401157.
- [82] Y. Zhang, S. Almenabawy, G. Vytas, M. Shayegannia, J. Shen, H. Wang, N. P. Kherani, Adv. Opt. Mater. 2025, 13, 2402772.
- [83] T. Bajpai, S. Tripathi, IEEE Electron. Device Lett. 2025, 46, 1377.
- [84] M. Li, C. Wu, M. Chen, T. Weng, X. Yu, K. Lin, Y. Cao, X. Yu, Z. Li, Q. Qiao, H. Zhang, Y. Zhou, ACS Appl. Mater. Interfaces 2024, 16, 12754.
- [85] Z. Liu, L. Tao, Y. Zhang, G. Zhou, H. Zhu, Y. Fang, G. Wu, D. Yang, H. Chen, Adv. Opt. Mater. 2021, 9, 2100288.
- [86] J. Han, W. Deng, F. Hu, S. Han, Z. Wang, Z. Fu, H. Zhou, H. Yu, J. Gou, J. Wang, Adv. Funct. Mater. 2025, 35, 2423360.